High-fidelity state transfer in silicon-vacancy-phononic networks with closed mechanical subsystems

Weihu Xu [1], Juntao Li [1], Zeyang Liao [1,*] and Xiaoqi Zhou [1,2,†]
[1] *State Key Laboratory of Optoelectronic Materials and Technologies and School of Physics, Sun Yat-sen University, Guangzhou 510000, China*
[2] *Hefei National Laboratory, Hefei 230088, China*

(Received 2 December 2025; accepted 19 October 2026; published 9 November 2026)

Building on the alternating-waveguide closed-mechanical-subsystem architecture introduced by Kuzyk and Wang [Phys. Rev. X **8**, 041027 (2018)], we develop a diamond phononic network that overcomes the coupling-hierarchy bottleneck in the implementation analyzed there. Beyond replacing nitrogen-vacancy centers with silicon-vacancy (SiV) centers, we independently engineer the two relevant couplings: Localized defect modes and strong SiV orbital-strain interaction enhance the spin-phonon coupling G, whereas cavity-waveguide engineering suppresses the cavity-waveguide coupling g. The resulting coupling hierarchy reverses that found in earlier physical implementations of closed-mechanical-subsystem networks and places the system in the $G \gg g$ regime required for direct state transfer. This hierarchy reversal qualitatively changes the appropriate control strategy from bichromatic Mølmer-Sørensen driving to a simple direct triple swap. Within our model, the resulting protocol enables state transfer with a fidelity of 0.999 on a microsecond timescale and remains robust against mechanical dissipation, spin dephasing, and finite thermal occupation. Our results establish a distinct route for scalable solid-state phononic quantum networks.

DOI: 10.1103/d3p6-yxps

I. INTRODUCTION

Phonons—the quanta of mechanical vibrations—are attractive carriers for on-chip quantum information processing [1–12]. Unlike electromagnetic waves, mechanical waves do not propagate in vacuum and are therefore immune to radiative loss. Moreover, their slow propagation speed allows long wavelengths to be achieved at relatively low frequencies, offering additional advantages. Phonon quantum networks have emerged as scalable platforms capable of interfacing with diverse solid-state qubits [3,4,10,11,13]. Acoustic-wave interactions with quantum systems have been demonstrated in several platforms, including quantum dots [14–20], superconducting circuits [21–26], and diamond spin defects such as nitrogen-vacancy (NV) and silicon-vacancy (SiV) centers [8,9,11,12,27–35]. Notably, diamond color centers provide a natural optical interface for integrated diamond nanophotonics and quantum-optical networks [8,12,32,33]. SiV-based optomechanics/phononics is already an active research area, including SiV phonon networks, hybrid phononic interfaces, coherent SiV spin control, and spin-phonon interactions in phononic or optomechanical crystals [3,6,11,12,33–35].

We investigate the coupling between SiV centers and phononic crystal defect cavities. In systems such as NV centers, where the relevant ground-state sublevels reside within the same orbital branch, the strain susceptibility is relatively weak, typically on the order of 10^9 Hz per unit (dimensionless) strain [36–38]. In contrast, for SiV centers whose low-energy manifold involves distinct orbital branches, the orbital strain susceptibility can be as large as $\sim 10^{15}$ Hz per unit strain [39–41]. Introducing a defect into the periodic structure gives rise to a high-quality-factor defect cavity that tightly confines the mechanical modes [6,12,42,43].

Large-scale mechanical networks face significant challenges in scalability. For example, in trapped-ion quantum computers, the coupling among multiple vibrational modes leads to dense spectra and unwanted crosstalk, which constrains quantum control and gate operation speed [44]. To overcome these challenges, a closed-mechanical-subsystem architecture has been proposed, in which a large mechanical network is divided into isolated, independently controllable subsystems [4,5]. Within these subsystems, high-fidelity quantum state transfer and two-qubit gates can be achieved via phonon-mediated interactions [4,45].

Quantum state transfer between adjacent nodes can be achieved through a triple-swap process, which, in NV center-based systems, requires the spin-resonator coupling strength G to greatly exceed the resonator-waveguide coupling strength g [4]. However, in practical implementations [4,5], material and structural limitations generally lead to the condition $G \ll g$. Consequently, more sophisticated control techniques are required to realize high-fidelity state transfer via the Mølmer-Sørensen gate. Thus, in such architectures the triple-swap protocol is not practically implementable.

*Contact author: liaozy7@mail.sysu.edu.cn
†Contact author: zhouxq8@mail.sysu.edu.cn

Published by the American Physical Society under the terms of the Creative Commons Attribution 4.0 International license. Further distribution of this work must maintain attribution to the author(s) and the published article's title, journal citation, and DOI.

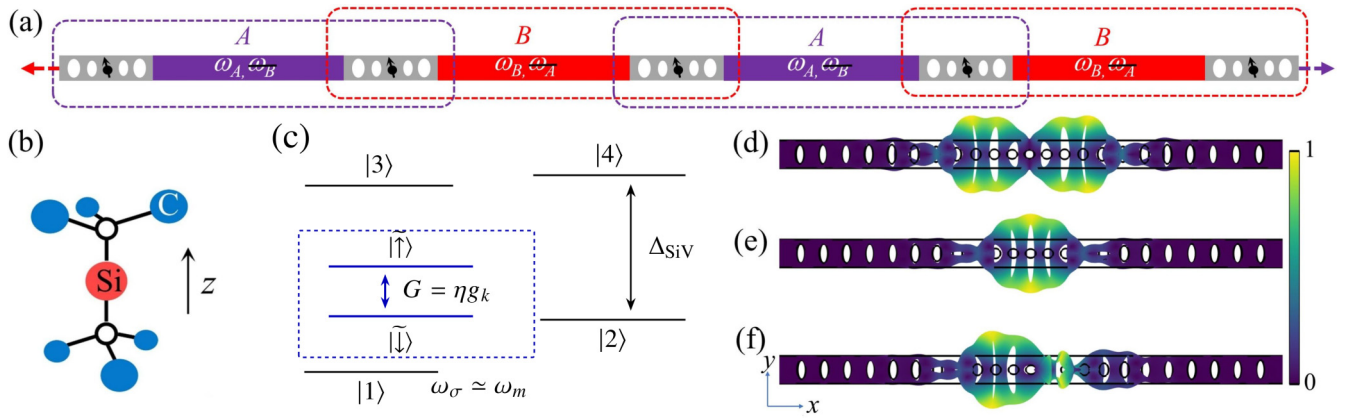


FIG. 1. (a) Schematic of the phononic network. Each phononic crystal defect cavity is coupled to two distinct phononic crystal waveguides, labeled A and B, which support phonon modes centered at ω_A and ω_B, respectively. Within each defect cavity, an SiV-center spin interacts selectively with two localized mechanical modes corresponding to ω_A and ω_B. Atomic structure [panel (b)] and field- and strain-dressed low-energy spin-phonon interface [panel (c)] of the SiV center. In panel (c), Δ_{SiV} denotes the bare orbital splitting, and $G = \eta g_k$ couples the dressed states $|\widetilde{\downarrow}\rangle$ and $|\widetilde{\uparrow}\rangle$ resonantly when $\omega_\sigma \simeq \omega_m$. (d)–(f) Displacement fields of the third-, first-, and second-order localized modes of the cavity, with frequencies of $\omega_A/2\pi = 11.941$ GHz, $\omega_B/2\pi = 11.514$ GHz, and $\omega_C/2\pi = 11.613$ GHz, respectively.

In this work, building on the alternating-waveguide closed-mechanical-subsystem architecture introduced previously [4], we overcome the coupling-hierarchy bottleneck in earlier physical implementations [4,5]. The central advance is not a new architecture or protocol, but a reversal of the coupling hierarchy achieved by engineering the two relevant couplings through different mechanisms: Localized defect modes and strong SiV orbital-strain interaction enhance the spin-phonon coupling G, whereas cavity-waveguide engineering suppresses the cavity-waveguide coupling g. Finite-element simulations confirm that the resulting design preserves the frequency-selective closed mechanical subsystems while realizing the required coupling hierarchy. The resulting $G \gg g$ regime enables direct triple-swap state transfer without bichromatic Mølmer-Sørensen control. Within our model, the protocol achieves a fidelity of 0.999 on a microsecond timescale and remains robust against mechanical dissipation, spin dephasing, and finite thermal occupation. The scheme offers a feasible chip-scale platform for scalable phononic networks with solid-state spins.

This architecture is intended as a chip-scale phononic quantum interconnect rather than a stand-alone quantum memory or sensing register: The mechanical modes are only transiently populated and act as a quantum bus for state transfer, routing, and entanglement distribution.

II. PHONONIC QUANTUM NETWORK

As illustrated in Fig. 1(a), each phononic crystal defect cavity is connected to two independent phononic crystal waveguides, labeled A and B, which support phonon propagation at center frequencies ω_A and ω_B, respectively, while their band-gap structures are designed to suppress transmission at the opposite frequency. Consequently, any two adjacent defect cavities, together with the connecting waveguide, form a closed mechanical subsystem. For the SiV-center spin quantum nodes, each spin is designed to couple selectively to distinct localized mechanical modes of the defect cavity, corresponding to the transmission modes of waveguides A and B, as shown in Fig. 1(a). High-quality SiV centers can be realized in diamond via ion implantation [44–47]. Through these frequency-separated closed mechanical subsystems, fast and high-fidelity quantum state transfer between neighboring quantum nodes can be achieved.

A. Model

The SiV center is a point defect in diamond consisting of a silicon atom located symmetrically between two adjacent carbon vacancies, forming a split-vacancy configuration [3,48,49]. Its electronic ground state hosts an unpaired hole with an effective spin $S = 1/2$, as illustrated in Fig. 1(b). Owing to strong spin-orbit coupling, the ground state is divided into two orbital branches separated by $\Delta_{\mathrm{SiV}}/2\pi \approx 46$ GHz. When an external magnetic field is applied, each orbital branch further splits into two spin sublevels, denoted as $|1\rangle = |e_-, \downarrow\rangle$, $|2\rangle = |e_+, \uparrow\rangle$, $|3\rangle = |e_+, \downarrow\rangle$, and $|4\rangle = |e_-, \uparrow\rangle$, as shown in Fig. 1(c). The orbital states $|e_\pm\rangle$ are eigenstates of the orbital angular momentum operator $\hat{L}_z$, satisfying $\hat{L}_z|e_\pm\rangle = \pm|e_\pm\rangle$. Lattice deformations from a localized mechanical mode shift the SiV orbital energies, generating strain-mediated coupling between the phonon mode and the orbital degrees of freedom [3,41,50]. With $\hat{a}$ denoting the mechanical-mode annihilation operator and g_k the bare coupling strength, the interaction Hamiltonian is [3,34,51,52]

$$\hat{H}_{\mathrm{strain}} = g_k(|3\rangle\langle 1| + |4\rangle\langle 2|)\hat{a} + \mathrm{H.c.} \tag{1}$$

The coupling is

$$g_k = \frac{d}{v}\sqrt{\frac{\hbar\omega_k}{2\rho V}}\,\xi(\mathbf{r}_{\mathrm{SiV}}). \tag{2}$$

Here, $d/2\pi \approx 1$ PHz/strain is the strain susceptibility, $v \approx 10^4$ m/s is the acoustic group velocity in diamond, $\rho \approx 3500$ kg/m^3 is the mass density, V is the defect-cavity volume, ω_k is the mechanical-mode frequency, and $\xi(\mathbf{r}_{\mathrm{SiV}})$ is the

strain profile at the SiV position. For the 11–12 GHz modes considered here, a transverse magnetic field and static strain admix orbital character into two low-energy SiV eigenstates, denoted by $|\widetilde{\downarrow}\rangle$ and $|\widetilde{\uparrow}\rangle$ [6,7,12,41]. Projecting $\hat{H}_{\text{strain}}$ onto this dressed-spin subspace gives

$$\hat{H}_{\text{int}} = G(\hat{\sigma}_+\hat{a} + \text{H.c.}), \tag{3}$$

where $\hat{\sigma}_+ = |\widetilde{\uparrow}\rangle\langle\widetilde{\downarrow}|$, $G = \eta g_k$, $\eta = |\langle\widetilde{\uparrow}|\hat{J}_+|\widetilde{\downarrow}\rangle|$, and $\hat{J}_+ = |3\rangle\langle 1| + |4\rangle\langle 2|$ raises the energy within each bare spin sector. Here, η quantifies the orbital character of the dressed spin transition. In the interaction picture, the exchange term is proportional to $\exp[i(\omega_\sigma - \omega_m)t]$ and is therefore resonant when $\omega_\sigma \simeq \omega_m$. Thus, the 11–12 GHz frequencies in Figs. 1(d)–1(f) are the mechanical-mode frequencies and the corresponding resonantly matched dressed-spin transition frequencies. The bare orbital splitting $\Delta_{\text{SiV}}/2\pi \simeq 46$ GHz determines the dressed-state composition and strain matrix element, but it is not bridged directly by the mechanical mode.

B. Strong spin-phonon coupling

We use finite-element simulations to compute mechanical eigenmodes and band structures for the phononic crystal cavity-waveguide network. Eigenmodes are calculated with perfectly matched layers (PMLs) at both ends (with the outer PML boundaries fixed), and band structures are obtained from a single unit cell with periodic boundary conditions.

We simulate the phononic crystal defect cavity with structural parameters adapted from experimental reports [53–55]. As illustrated in Fig. 2(a), the primitive unit cell of the phononic crystal consists of a diamond-shaped block perforated by an elliptical hole. The corresponding mechanical band structure, shown in Fig. 2(c), exhibits several acoustic branches within the gigahertz range, which are classified according to their displacement symmetries. Following previously established design principles, we focus on the mechanical breathing mode located at the Γ point of the Brillouin zone. Figure 2(d) illustrates the evolution of this breathing-mode frequency as the unit cell geometry is gradually transformed from the structure in Fig. 2(a) to that in Fig. 2(b). Reducing both the lattice constant a and the hole aspect ratio $r_h = h_y/h_x$ lowers the mechanical frequency at the Γ point, pushing the mode into the quasi-band-gap region indicated by the shaded area in Fig. 2(c). This gradual transition defines a defect cavity, as depicted by the spatial variation of the cell parameters in Fig. 2(e), and the resulting two-dimensional (2D) structure is shown schematically in Fig. 2(f).

The designed defect cavity supports multiple strongly localized mechanical modes. Figures 1(d)–1(f) show the simulated displacement distributions of the first-, second-, and third-order localized modes in the cavity. At the selected SiV position, finite-element simulations yield bare orbital-phonon coupling strengths of $g_{k,A}/2\pi = 30.7$ MHz and $g_{k,B}/2\pi = 32.2$ MHz for modes A and B, respectively. The corresponding spatial distributions are shown in Fig. 3; details of the zero-point normalization and strain projection are provided in Appendix C.

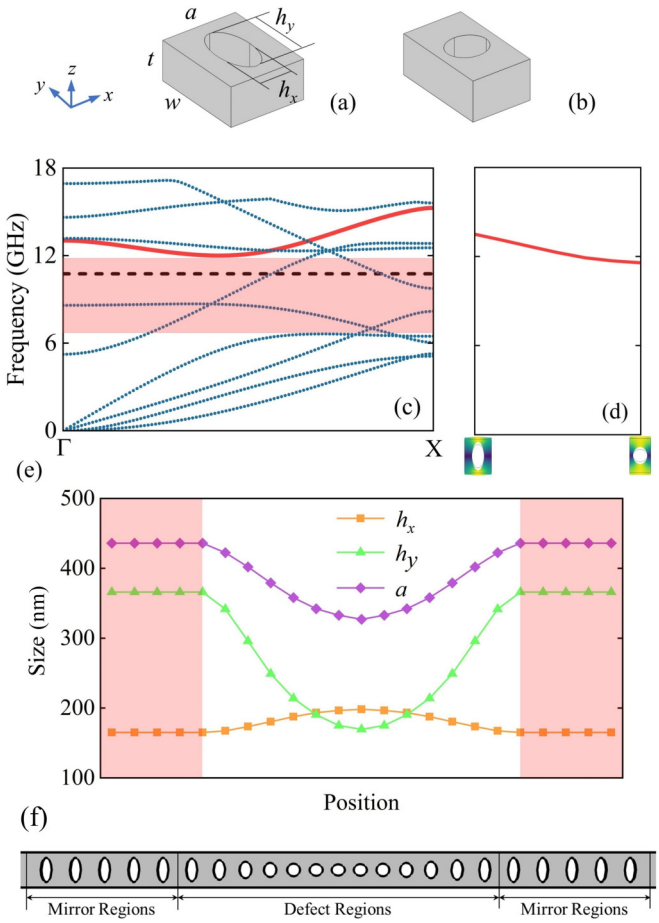


FIG. 2. The structural design and mechanical properties of the proposed phononic crystal defect cavity. (a) Dimensions of the nominal unit cell, defined as $(a, t, w, h_x, h_y) = (422.4, 220, 529, 167.3, 341.6)$ nm. The defect cell parameters are $(a, t, w, h_x, h_y) = (327, 220, 529, 198.1, 169.5)$ nm, as shown in panel (b). (c) Mechanical band structure, with the breathing-mode branch highlighted in red. The shaded quasi-band-gap excludes modes of the same symmetry but contains modes of other symmetries; the black dashed line marks the defect-cavity frequency. All mechanical simulations are performed using the anisotropic elasticity tensor of diamond with stiffness constants $(C_{11}, C_{12}, C_{44}) = (1076, 125, 578)$ GPa. As illustrated in panel (d), the mechanical mode at the Γ point can be tuned continuously by smoothly transforming the unit cell geometry from the nominal configuration to the defect cell. (e) The gradual variation of the key structural parameters—lattice constant a (purple), h_x (orange), and h_y (green)—along the cavity axis. (f) A 2D schematic of the complete defect cavity.

C. Closed mechanical subsystems

To construct closed mechanical subsystems, we introduce two alternating phononic crystal waveguides, labeled A and B. Each unit contains an SiV-embedded phononic crystal defect cavity linked to waveguides A and B with different lattice periods [Fig. 4(a)]. Both waveguides exhibit acoustic band gaps for symmetric mechanical modes, whose displacement profiles are symmetric with respect to the y and z axes, with the band gap of waveguide B centered at a higher frequency [Fig. 4(b)]. Although modes of other symmetry classes exist in

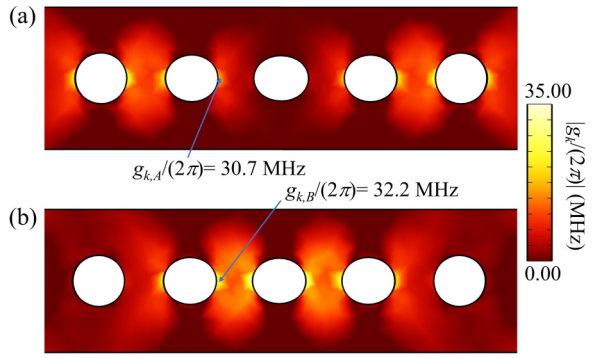


FIG. 3. Spatial maps of the bare SiV orbital-phonon coupling $|g_{k,\mu}(\mathbf{r})|/2\pi$ for modes A (11.941 GHz, upper) and B (11.514 GHz, lower). The arrows indicate the selected SiV site, where $|g_{k,A}|/2\pi = 30.7$ MHz and $|g_{k,B}|/2\pi = 32.2$ MHz; both panels use the same color scale.

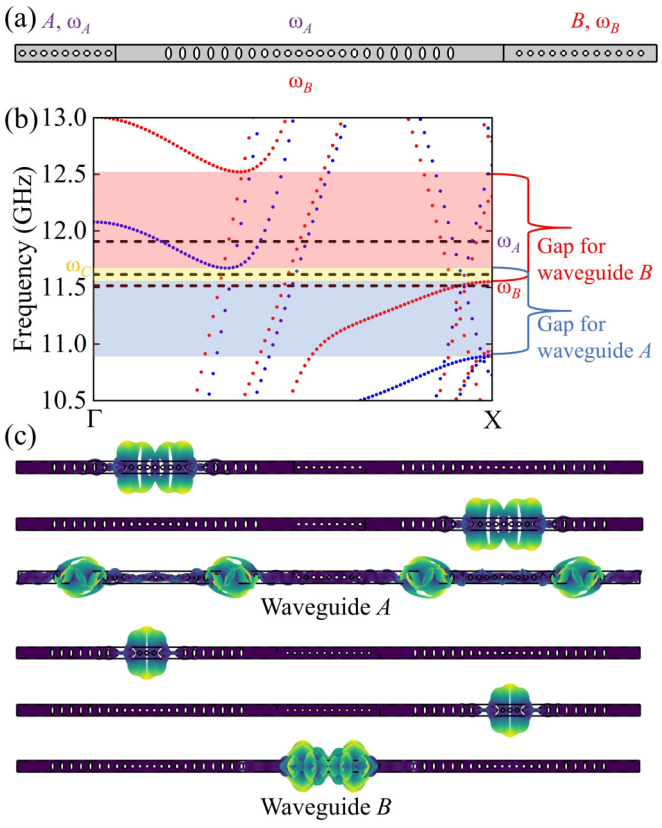


FIG. 4. (a) The phononic crystal defect cavity is coupled to waveguides A and B. (b) The phononic band structures of waveguides A (blue) and B (red). Both waveguides exhibit acoustic band gaps for symmetric mechanical modes, whose displacement distributions are symmetric with respect to the y and z axes. Blue (red) shading denotes the nonoverlapping band gap of waveguide A (B); yellow denotes their overlap. Dashed lines denote the resonance frequencies ω_A and ω_B of the defect cavity modes coupled to their respective waveguide modes. (c) Displacement distributions of the normal-mode triplets for the closed mechanical subsystems associated with waveguides A and B.

the same frequency range, the symmetric mechanical modes are completely suppressed within the shaded regions, giving rise to sizable symmetry-resolved band gaps. These nonoverlapping spectral regions [red and blue in Fig. 4(b)] ensure that modes in the upper band propagate only in waveguide A, whereas those in the lower band propagate only in waveguide B. The defect cavity's third-order localized mode at $\omega_A/2\pi = 11.941$ GHz lies within the band gap of waveguide B and couples resonantly to a propagating mode in waveguide A. Similarly, the first-order localized mode at $\omega_B/2\pi = 11.514$ GHz lies within the band gap of waveguide A and couples to a propagating mode in waveguide B. This arrangement ensures that each adjacent pair of defect cavities and their connecting waveguide form a closed mechanical subsystem, thus realizing the modular architecture shown in Fig. 1. The second-order localized mode at $\omega_C/2\pi = 11.613$ GHz corresponds to the yellow-shaded region in Fig. 4(b).

D. Weak cavity-waveguide coupling

For a closed mechanical subsystem comprising two adjacent defect cavities connected by a waveguide, the cavity-waveguide coupling leads to the formation of three normal modes. In the single-mode waveguide limit, the cavity-waveguide coupling rate g can be calculated from the numerically obtained normal-mode frequencies using the method described in Ref. [4]:

$$g = \sqrt{\frac{(\omega_+ - \omega')(\omega' - \omega_-)}{2}}. \tag{4}$$

Here, ω_+, ω_-, and ω' denote the eigenfrequencies of the three normal modes.

For waveguide lengths of $L_A = 3.1$ μm and $L_B = 4.7$ μm, the localized modes shown in Figs. 1(d) and 1(e) are found to be resonant or near-resonant with their respective waveguide modes. Waveguide A has unit cells characterized by a lattice constant of 332.8 nm and elliptical holes with minor and major axes of 184.5 and 163 nm, respectively, while waveguide B features a lattice constant of 342.1 nm and elliptical holes with minor and major axes of 157.4 and 154.3 nm. For the finite-length waveguide segments connecting adjacent defect cavities, the simulated frequency spacing between neighboring guided modes is 78 MHz in waveguide A and 53 MHz in waveguide B, as obtained from independent waveguide calculations without coupling to the defect cavities.

The strongly localized mechanical modes of the defect cavity efficiently suppress acoustic leakage, leading to a substantial reduction in the cavity-waveguide coupling rate g. Figure 4(c) presents the displacement distributions of the normal-mode triplets within the closed mechanical subsystem, with frequencies (from top to bottom) corresponding to ω_-, ω', and ω_+ for both waveguides A and B. The extracted coupling strengths are $g_A = 0.12$ MHz and $g_B = 0.14$ MHz. Further optimization of the defect geometry allows fine-tuning of g without compromising the overall coupling efficiency, enabling precise control of the interaction strength. Our model satisfies the condition $G \gg g$.

In networks based on closed mechanical subsystems, only local resonance conditions must be satisfied [4,5]; as long as each subsystem remains internally resonant, the overall

architecture is robust against global or long-range frequency fluctuations.

E. Isolating intranode spin-phonon coupling from the waveguides

Following Ref. [4], we classify the SiV-center spin qubits embedded in the phononic crystal defect cavity into two functional types: computational qubits and communication qubits. The communication qubits mediate quantum state transfer between adjacent network nodes, while the computational qubits are dedicated to local information processing. Individual addressing can be implemented using strain-induced differences in the relevant microwave transition frequencies, as demonstrated for two SiV centers with a common symmetry axis under the same magnetic field in a single nanophotonic cavity [56]. In our scheme, this requires individual spectroscopic calibration and transition separations sufficiently large compared with the relevant linewidths, drive strengths, and pulse bandwidths. Shared defect-cavity modes could mediate local spin-spin interactions among the qubits within each node.

The phononic band-gap structure isolates the mechanical modes mediating these intranode interactions from the propagating waveguide modes, implementing the isolation strategy of Ref. [4]. Specifically, the computational qubits can couple to one another and to the communication qubit through a defect-cavity mode whose frequency lies within the overlapping band gap of the two phononic waveguides, indicated by the yellow-shaded region in Fig. 4(b). Under this condition, the phonon-mediated coupling between the computational and communication qubits is effectively decoupled from the adjacent waveguides, thereby suppressing phonon leakage and crosstalk.

As a concrete result of the present design, the second-order localized mode of the defect cavity, with a frequency of $\omega_C/2\pi = 11.613$ GHz, lies within the overlapping band gap of both waveguides and therefore provides a suitable mechanical channel for intranode spin-phonon coupling. Other defect-cavity modes within similar spectral overlap regions may also be used, providing additional flexibility in the physical allocation of computational qubits.

F. Nanoscale two-dimensional phononic shield

Two-dimensional phononic shielding has previously been proposed for closed-subsystem networks [4]. Here, we embed the present nanoscale cavity-waveguide device in a two-dimensional phononic crystal to suppress environmental perturbations and mechanical energy leakage, as illustrated in Fig. 5(a).

Previous work has demonstrated that 2D phononic crystals can effectively isolate mechanical systems, such as optomechanical crystals, membranes, and single-mode waveguides, from external dissipation channels [57–62]. This approach has enabled experimental realizations of exceptionally high mechanical quality factors Q_m, with $\omega Q_m/2\pi$ values reaching or even exceeding 10^{17} Hz [59–62].

For the present device, the calculated phononic band structure in Fig. 5(b) exhibits a complete band gap from 8.9 to 13.5 GHz, fully covering the operating frequencies and band

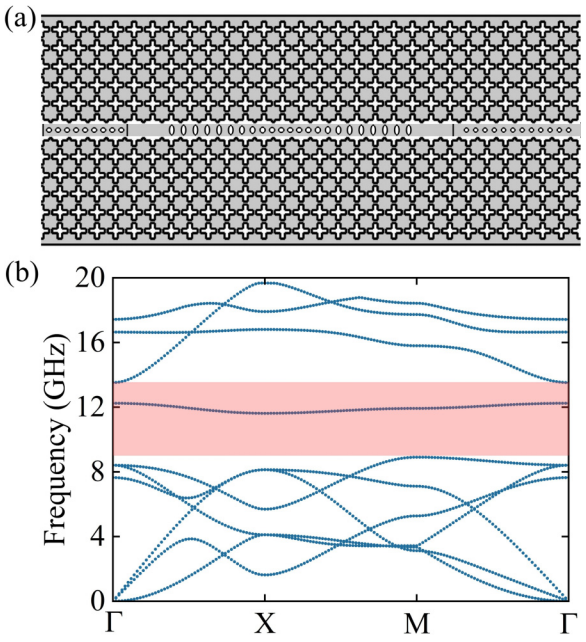


FIG. 5. (a) The fundamental components of the phononic network are integrated into a square phononic crystal lattice with a lattice period of 614 nm. Each square unit cell has a side length of 454 nm and is connected to adjacent cells by bridges 160 nm long and 134 nm wide. (b) Phononic band structure of the designed 2D lattice.

gaps of waveguides A and B. This complete band gap suppresses the propagation of the relevant mechanical modes into the surrounding crystal, thereby reducing their coupling to external mechanical channels. The proposed configuration of defect cavities, waveguides, and phononic shields is not optimized, but rather serves as a representative design demonstrating the feasibility of the phononic network architecture.

III. COUPLING-HIERARCHY REVERSAL AND DIRECT TRIPLE-SWAP STATE TRANSFER

Phononic and optomechanical interfaces for quantum information processing have been widely investigated [2,3,6,7,11,12,34,63–67]. The previously established triple-swap protocol requires $G/g \gg 1$ for high-fidelity operation [4], whereas earlier closed-subsystem designs operate in the opposite $G \ll g$ regime [4,5]. Here, we overcome this coupling-hierarchy bottleneck, enabling direct triple-swap state transfer without bichromatic Mølmer-Sørensen control.

A. Model and operating parameters

The closed mechanical subsystem discussed above consists of three mechanical modes: two localized defect cavity modes with annihilation operators $\hat{a}_1$ and $\hat{a}_2$, and a waveguide mode $\hat{b}$. For simplicity, we assume identical cavity-waveguide coupling g and that all three modes share the same resonance frequency. Small deviations from exact resonance only weakly affect the triple-swap dynamics and can be compensated by tuning [4]. Each localized defect cavity mode interacts with a single SiV-center spin. The interaction

TABLE I. Comparison with Ref. [4]. Values for modes A/B are listed in that order. Different protocols and noise models preclude direct performance benchmarking.

Quantity	Reference [4]	This work
$G/2\pi$ (MHz)	$\simeq$0.1[a]	$\simeq$6
$g/2\pi$ (MHz)	$\sim$1 to $>$10	0.12/0.14
G/g	$\sim$0.01–0.1	50/42.9
Transfer time (μs)	Not reported	3.03/2.61
Fidelity	$>$0.99 (gate)[b]	$\simeq$0.999 (transfer), $G/g = 40$
Control	Bichromatic drive + single-qubit operations	Sequential resonant switching

[a]Representative coupling estimate.
[b]Mølmer-Sørensen gate fidelity for $G/2\pi \gtrsim 0.23$–0.32 MHz under the conditions specified in Ref. [4].

Hamiltonian governing quantum state transfer between the two spins can then be written as

$$\hat{H}_I = \hbar g \hat{b}^\dagger(\hat{a}_1 + \hat{a}_2) + \hbar[G_1(t)\hat{\sigma}_+^1\hat{a}_1 + G_2(t)\hat{\sigma}_+^2\hat{a}_2] + \text{H.c.}, \tag{5}$$

where $G_1(t)$ and $G_2(t)$ are the time-dependent effective spin–phonon couplings. Each SiV spin couples selectively to a specific localized cavity mode. For each localized mode $\mu \in \{A, B\}$, we assume a resonant dressed SiV transition, $\omega_{\sigma,\mu} = \omega_\mu$. The calculated bare couplings are $g_{k,A}/2\pi = 30.7$ MHz and $g_{k,B}/2\pi = 32.2$ MHz. Taking $\eta_\mu = 0.2$ as a model parameter gives $G_A/2\pi = 6.14$ MHz and $G_B/2\pi = 6.44$ MHz; the transfer simulations use the common approximation $G/2\pi = 6$ MHz. We model spin-phonon exchange as controlled by local strain tuning of the dressed SiV transition [12]. Exchange is enabled at $\omega_{\sigma,\mu} = \omega_\mu$ and suppressed when $|\omega_{\sigma,\mu} - \omega_\mu| \gg G_\mu$. The pulse envelopes $G_i(t)$ represent the resulting idealized resonant-swap intervals: We assume instantaneous switching and neglect residual off-resonant exchange. Local strain can shift SiV transition frequencies [41], while fabrication variations can alter spin-phonon couplings; both require node-resolved calibration. The normal-mode splittings yield $g_A/2\pi = 0.12$ MHz and $g_B/2\pi = 0.14$ MHz. Together with $G/2\pi \simeq 6$ MHz, these values correspond to $G/g_A = 50$ and $G/g_B = 42.9$. Table I compares the coupling hierarchy and control requirements of our design with those of Ref. [4], alongside their respective reported performance metrics.

Under realistic conditions, we include the mechanical dissipation and thermal noise of all three mechanical modes, as well as spin dephasing. For simplicity, we assume the same mechanical damping rate κ and thermal occupation n_{th} for the two localized cavity modes and the waveguide mode. The system dynamics follow the master equation

$$\dot{\rho} = -i[\hat{H}_I, \rho] + \sum_{\mu=1}^{3}[(n_{\text{th}}+1)\kappa\mathcal{D}[\hat{c}_\mu]\rho + n_{\text{th}}\kappa\mathcal{D}[\hat{c}_\mu^\dagger]\rho] + \Gamma\sum_{j=1}^{2}\mathcal{D}[\hat{\sigma}_z^j]\rho, \tag{6}$$

where $\hat{c}_1 = \hat{a}_1$, $\hat{c}_2 = \hat{a}_2$, and $\hat{c}_3 = \hat{b}$. Here, $\mathcal{D}[o]\rho = 2o\rho o^\dagger - \rho o^\dagger o - o^\dagger o\rho$ is the Lindblad dissipator. The mechanical Lindblad terms describe the damping and thermal excitation of the two localized cavity modes and the waveguide mode. For the shielded mechanical modes, our simulations yield a radiation-limited quality factor $Q_{\text{rad}} \sim 10^{13}$, giving $\kappa_{\text{rad}}/2\pi = (\omega_m/2\pi)/Q_{\text{rad}} \sim 1$ mHz, where ω_m is the mode angular frequency and κ_{rad} is the radiative energy decay rate. This estimate describes the ideal radiation-loss limit, not the total damping of a fabricated device. For the assumed equilibrium bath, thermal excitation is weak over the transfer timescale. The long SiV coherence time at 100 mK reported in Ref. [68] relies on dynamical decoupling. We adopt $\kappa/2\pi = 10^{-3}$ Hz and $\Gamma/2\pi = 100$ Hz as numerical benchmarks; the latter is an assumed dephasing rate for simulations without dynamical decoupling.

B. Triple-swap dynamics

As illustrated in Fig. 6(a), the quantum state transfer between two spin qubits is implemented via a triple-swap protocol. Spin 1 is initialized in $|2\rangle$, spin 2 is fixed in $|1\rangle$, and the mechanical modes are prepared in the vacuum state $|0, 0, 0\rangle$. At $T = 0.1$ K, the 11.5–11.9 GHz modes have equilibrium occupations of $\simeq$0.003–0.004, but absorption-induced heating during optical initialization can increase them [59]. Two-dimensional optomechanical crystals can mitigate this heating via out-of-band phonon transport while retaining band-gap isolation of the target mode [69]. The assumed vacuum initial state requires sufficiently low residual mechanical occupation after initialization. In the first swap, we set $G_2 = 0$ and activate G_1 for a duration $\tau_1 = \pi/(2G_1)$, mapping the excitation of spin 1 onto the phonon mode $\hat{a}_1$. During the second swap, both spin-phonon couplings are turned off ($G_1 = G_2 = 0$), allowing complete excitation transfer from $\hat{a}_1$ to $\hat{a}_2$ via the waveguide in $\tau_2 = \pi/(\sqrt{2}g)$ [70]. The waveguide mode is transiently populated but returns to vacuum at the end of the swap. In the final swap, we set $G_1 = 0$ and apply G_2 for $\tau_3 = \pi/(2G_2)$, transferring the excitation from $\hat{a}_2$ to spin 2. Overall, the triple-swap sequence transfers the state from spin 1 to spin 2. For $G_1 = G_2 = G$, the total transfer time is

$$T_{\text{tr}} = \tau_1 + \tau_2 + \tau_3 = \frac{\pi}{G} + \frac{\pi}{\sqrt{2}g}. \tag{7}$$

The coupling values give $T_{\text{tr}} = 3.03$ μs for transfer through waveguide A and $T_{\text{tr}} = 2.61$ μs for transfer through waveguide B. For the simulations below, we set $G_1 = G_2 = G$ and adopt the conservative common value $G/g = 40$. Each spin-phonon swap lasts $\simeq$42 ns; between swaps, the information resides in the mechanical modes, with both spins ideally in their

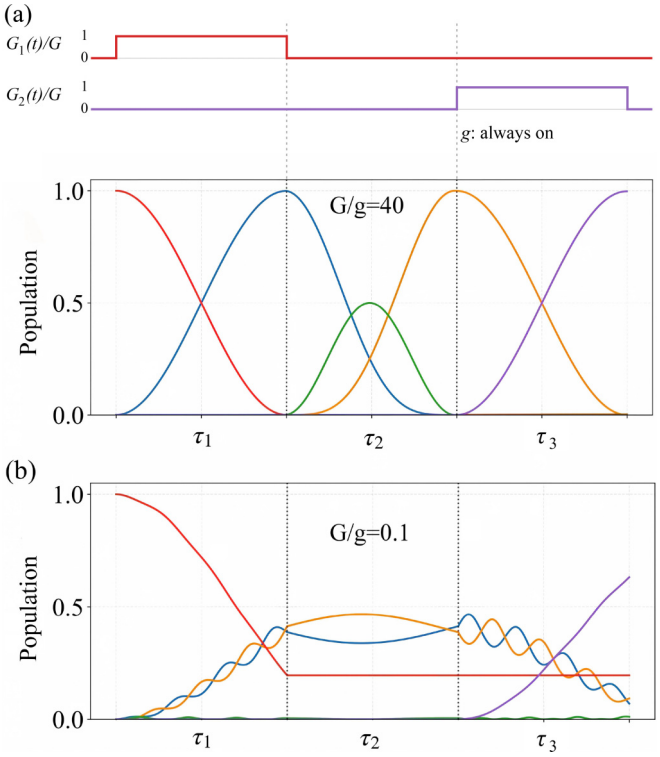


FIG. 6. Population dynamics of the triple-swap sequence for two coupling hierarchies. (a) Dynamics at the conservative operating point $G_1 = G_2 = G$ and $G/g = 40$. The pulse sequence in panel (a) shows $G_1(t)$ and $G_2(t)$; the cavity-waveguide coupling g remains on throughout. The three stages are plotted with separately scaled time axes. (b) Dynamics at $G/g = 0.1$, the upper end of the representative single-spin range estimated in Ref. [4]. The curves represent defect-cavity modes 1 (blue) and 2 (orange), the waveguide mode (green), and spins 1 (red) and 2 (purple). Dissipation and dephasing are omitted to isolate the effect of the coupling hierarchy.

ground states. No additional decoupling pulses are included, as they would generally modify the exchange interaction. For comparison, Fig. 6(b) shows the same triple-swap sequence at $G/g = 0.1$, the upper end of the representative single-spin range estimated in Ref. [4]. Even without dissipation or dephasing, dominant cavity-waveguide coupling disrupts spin-cavity swaps, preventing complete transfer. This comparison isolates the effect of the coupling hierarchy within the same triple-swap protocol.

C. Transfer fidelity and robustness

During the spin-cavity swaps (the first and third steps), unavoidable coupling to the waveguide mode limits the overall state-transfer fidelity

$$\mathcal{F} = \left\{ \mathrm{Tr}\left[(\sqrt{\rho(t_f)} U_{\mathrm{SWAP}} \rho(t_i) U_{\mathrm{SWAP}}^{+} \sqrt{\rho(t_f)})^{1/2} \right] \right\}^2, \quad (8)$$

where U_{SWAP} denotes the ideal two-qubit SWAP operation and ρ is the reduced two-qubit density matrix [71]. Consistent with Ref. [4], Fig. 7(a) recovers the generic dependence of the triple-swap fidelity on G/g. At the conservative operating point $G/g = 40$, the stated model gives $\mathcal{F} \simeq 0.999$. Figure 7(b) further quantifies the fidelity as a function of the

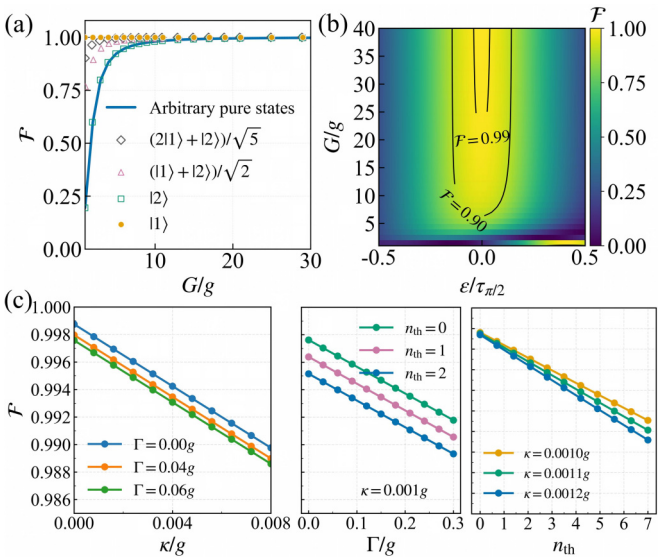


FIG. 7. State-transfer fidelity and robustness of the triple-swap protocol. (a) Minimum fidelity over all pure input states of spin 1 vs G/g; selected input states are shown for comparison. (b) Fidelity vs the normalized pulse-duration deviation $\varepsilon/\tau_{\pi/2}$ and G/g. (c) Fidelity vs the mechanical dissipation rate κ (left), spin-dephasing rate Γ (middle), and thermal phonon occupation n_{th} (right), evaluated at $G/g = 40$.

normalized pulse-duration deviation $\varepsilon/\tau_{\pi/2}$, where $\varepsilon = \tau - \tau_{\pi/2}$ and $\tau_{\pi/2} = \pi/(2G)$, including the device-relevant $G/g = 40$ regime. For smaller G/g, the maximum fidelity occurs at a nonzero pulse deviation because the cavity-waveguide coupling remains active during the transfer, whereas it approaches $\varepsilon = 0$ in the limit $G/g \gg 1$.

Figure 7(c) shows the fidelity versus the mechanical dissipation rate κ, the dephasing rate Γ, and the thermal phonon occupation n_{th}. We vary κ from $0.001g$ to $0.008g$, corresponding to $\kappa/2\pi \simeq 0.12$–1.12 kHz for the present device parameters, to assess the robustness of the protocol against mechanical damping far exceeding the radiation-loss limit. We vary Γ from $0.03g$ to $0.3g$, well above the benchmark value. We also vary the bath occupation n_{th} from 1 to 7, well above its equilibrium value at $T = 0.1$ K. The fidelity remains around 0.99 over the noise ranges considered. Independent scans of sidewall and transverse position errors yield $\mathcal{F}_{\mathrm{min}} \geqslant 0.986$ within ± 1 nm. Larger deviations require postfabrication tuning (see Appendix E).

IV. CONCLUSIONS

In summary, building on the closed-mechanical-subsystem architecture and triple-swap protocol of Ref. [4], we present an SiV phononic-crystal design that reverses the coupling hierarchy of the implementation analyzed there. Localized defect modes and SiV orbital-strain interaction enhance the spin-phonon coupling G, while cavity-waveguide engineering suppresses the coupling g. The resulting $G \gg g$ hierarchy enables direct triple-swap state transfer without bichromatic Mølmer-Sørensen control. At the conservative operating point $G/g = 40$, our open-system model predicts a state-transfer fidelity of approximately 0.999 on a microsecond timescale,

while the protocol remains robust against mechanical dissipation, spin dephasing, and finite thermal occupation. The protocol remains robust to moderate fabrication errors, while optical-spring tuning offers a potential route to compensating larger frequency shifts [54]. The central advance is therefore access to the coupling hierarchy required for direct transfer, providing a distinct route toward scalable solid-state phononic quantum networks.

ACKNOWLEDGMENTS

This work was supported by the National Natural Science Foundation of China (Grant No. 62575313). X.Z. acknowledges support from the Quantum Science and Technology-National Science and Technology Major Project (Grant No. 2021ZD0300702). Z.L. acknowledges support from the National Key R&D Program of China (Grant No. 2021YFA1400800) and the Key Program of the National Natural Science Foundation of China (Grant No. 12334017).

DATA AVAILABILITY

There are no publicly available research data or software supporting this manuscript. Requests for further information or data should be sent to the authors.

APPENDIX A: ELECTRONIC STRUCTURE OF THE SiV CENTER

As discussed in the main text, the negatively charged SiV center in diamond possesses an electronic ground state containing a single unpaired hole with spin $S = 1/2$. This hole can occupy one of two degenerate orbital states, $|e_x\rangle$ and $|e_y\rangle$. Within this orbital doublet and under the influence of an external static magnetic field $\vec{B}$, the energy spectrum is governed by the combined effects of spin-orbit coupling, Jahn-Teller distortion, and Zeeman interactions. The effective Hamiltonian describing the system can be written as ($\hbar = 1$) [3,48,49]

$$\hat{H}_{\mathrm{SiV}} = -\lambda_{\mathrm{SO}} L_z S_z + \hat{H}_{\mathrm{JT}} + f\gamma_L B_z L_z + \gamma_s \vec{B}\cdot\vec{S}. \tag{A1}$$

Here, L_z and S_z are the projections of the dimensionless orbital and spin angular momentum operators $\vec{L}$ and $\vec{S}$ along the SiV symmetry axis, which is aligned with the z direction. $\lambda_{\mathrm{SO}} > 0$ denotes the spin-orbit coupling strength, γ_L and γ_s are the orbital and spin gyromagnetic ratios, respectively, and $f \approx 0.1$ accounts for the reduction of the orbital Zeeman contribution due to crystal-field effects. Within the ground-state manifold spanned by $|e_x\rangle$ and $|e_y\rangle$, only the operator L_z has nonzero matrix elements. For a magnetic field $\vec{B} = B_0\vec{z}$, Eq. (A1) can be recast in matrix form as

$$(\omega_Z - \lambda_{\mathrm{SO}} L_z)S_z + \hat{H}_{\mathrm{JT}} = \frac{1}{2}\begin{bmatrix} \omega_Z & i\lambda_{\mathrm{SO}} \\ -i\lambda_{\mathrm{SO}} & \omega_Z \end{bmatrix} \otimes \begin{bmatrix} 1 & 0 \\ 0 & -1 \end{bmatrix} + \begin{bmatrix} \Upsilon_x & \Upsilon_y \\ \Upsilon_y & -\Upsilon_x \end{bmatrix} \otimes \begin{bmatrix} 1 & 0 \\ 0 & 1 \end{bmatrix}. \tag{A2}$$

The axial-field eigenstates below have definite spin, so the orbital-strain interaction does not couple states of opposite spin. The dressed-spin interaction in Sec. II A instead requires transverse Zeeman mixing, which is included in Eq. (A1) but not evaluated in the axial-field solution. Accordingly, η is treated as a model parameter rather than calculated from the states below. Here, Υ_x and Υ_y denote the Jahn-Teller coupling strengths along the x and y directions, respectively, while $\omega_Z = \gamma_s B_0$ represents the spin Zeeman energy. For simplicity, the reduced orbital Zeeman term ($\sim f\gamma_L B_0$) is neglected, as it does not qualitatively affect the results discussed. Diagonalization of Eq. (A2) yields the four eigenstates

$$\begin{aligned} |1\rangle &= (\cos\theta|e_x\rangle - i\sin\theta e^{-i\phi}|e_y\rangle)|\downarrow\rangle, \\ |2\rangle &= (\cos\theta|e_x\rangle + i\sin\theta e^{i\phi}|e_y\rangle)|\uparrow\rangle, \\ |3\rangle &= (\sin\theta|e_x\rangle + i\cos\theta e^{-i\phi}|e_y\rangle)|\downarrow\rangle, \\ |4\rangle &= (\sin\theta|e_x\rangle - i\cos\theta e^{i\phi}|e_y\rangle)|\uparrow\rangle, \end{aligned} \tag{A3}$$

where

$$\tan(\theta) = \frac{2\Upsilon_x + \Delta_{\mathrm{SiV}}}{\sqrt{\lambda_{\mathrm{SO}}^2 + 4\Upsilon_y^2}}, \quad \tan(\phi) = \frac{2\Upsilon_y}{\lambda_{\mathrm{SO}}}. \tag{A4}$$

The corresponding eigenenergies are given by

$$E_{3,1} = (-\omega_Z \pm \Delta_{\mathrm{SiV}})/2, \quad E_{4,2} = (\omega_Z \pm \Delta_{\mathrm{SiV}})/2, \tag{A5}$$

with $\Delta_{\mathrm{SiV}} = \sqrt{\lambda_{\mathrm{SO}}^2 + 4(\Upsilon_x^2 + \Upsilon_y^2)} \approx 2\pi \times 46$ GHz. Since $\Upsilon_{x,y} \ll \lambda_{\mathrm{SO}}$ [3,48], the Jahn-Teller distortion induces only minor orbital mixing. Therefore, the eigenstates can be approximated as $|1\rangle \approx |e_-,\downarrow\rangle$, $|2\rangle \approx |e_+,\uparrow\rangle$, $|3\rangle \approx |e_+,\downarrow\rangle$, and $|4\rangle \approx |e_-,\uparrow\rangle$, corresponding to $\theta = \pi/4$ and $\phi = 0$.

APPENDIX B: QUANTIZATION OF THE DISPLACEMENT FIELD

In the main text, we consider a diamond phononic crystal defect cavity with a cross-sectional area A and total length $L \gg \sqrt{A}$. Within the frequency range of interest, the acoustic excitations can be modeled as elastic waves described by a displacement field $\vec{u}(\vec{r}, t)$ that obeys the equation of motion for a homogeneous, isotropic elastic medium [3,50]:

$$\rho\frac{\partial^2}{\partial t^2}\vec{u} = (\lambda + \mu)\vec{\nabla}(\vec{\nabla}\cdot\vec{u}) + \mu\vec{\nabla}^2\vec{u}. \tag{B1}$$

Expressed componentwise, this becomes

$$\rho\frac{\partial^2}{\partial t^2}u_k = (\lambda + \mu)\sum_m \frac{\partial^2 u_m}{\partial x_k \partial x_m} + \mu\sum_m \frac{\partial^2 u_k}{\partial x_m^2}. \tag{B2}$$

Here, ρ is the mass density, while λ and μ are the Lamé coefficients, given in terms of the Young's modulus E and the Poisson ratio ν as

$$\lambda = \frac{\nu E}{(1+\nu)(1-2\nu)}, \quad \mu = \frac{E}{2(1+\nu)}. \tag{B3}$$

For diamond, the material parameters used in both analytical calculations and finite-element simulations are $\rho = 3500\ \mathrm{kg/m^3}$, $E = 1050$ GPa, and $\nu = 0.2$.

Assuming periodic boundary conditions along the waveguide axis, the displacement field can be expanded as a

superposition of normal modes,

$$\vec{u}(\vec{r},t)=\frac{1}{\sqrt{2}}\sum_{k,n}\vec{u}^{\perp}_{n,k}(y,z)\left[A_{n,k}(t)e^{ikx}+A^{*}_{n,k}(t)e^{-ikx}\right], \quad \text{(B4)}$$

where $k=2\pi m/L$ is the longitudinal wave vector and n indexes the transverse phonon branches. Each mode amplitude $A_{n,k}(t)$ satisfies the harmonic equation $\ddot{A}_{n,k}(t)+\omega^2_{n,k}A_{n,k}(t)=0$, with eigenfrequency $\omega_{n,k}$ and transverse mode profile $\vec{u}^{\perp}_{n,k}(y,z)$ obtained numerically from Eq. (B1). The mode functions are orthogonal and normalized according to

$$\frac{1}{A}\int dydz\vec{u}^{\perp}_{n,k}\cdot\vec{u}^{\perp}_{\beta,k}=\delta_{n,\beta}. \quad \text{(B5)}$$

Equation (B1) can be derived from the elastic Lagrangian

$$L=\int d^3r\left[\frac{\rho}{2}\dot{\vec{u}}^2-\frac{(\lambda+\mu)}{2}\sum_{k,m}\frac{\partial u_k}{\partial x_m}\frac{\partial u_m}{\partial x_k}-\frac{\mu}{2}\sum_{k,m}\left(\frac{\partial u_k}{\partial x_m}\right)^2\right]. \quad \text{(B6)}$$

Substituting the normal-mode expansion of Eq. (B4), the total Lagrangian reduces to a collection of independent harmonic oscillators

$$L(\{Q_{n,k}\},\{\dot{Q}_{n,k}\})=\sum_{k,n}\frac{M}{2}\dot{Q}_{n,k}\dot{Q}_{n,-k}-\frac{1}{2}M\omega^2_{n,k}Q_{n,k}Q_{n,-k}, \quad \text{(B7)}$$

where $M=\rho AL$ is the effective mass and $Q_{n,k}=(A_{n,k}+A^{)}_{n,-k}/\sqrt{2}$. The corresponding canonical momentum is $P_{n,k}=\partial L/\partial\dot{Q}n,k=M\dot{Q}n,-k$, leading to the phonon Hamiltonian

$$\hat{H}_{\rm ph}=\sum_{k,n}\frac{P_{n,k}P_{n,-k}}{2M}+\frac{1}{2}M\omega^2_{n,k}Q_{n,k}Q_{n,-k}. \quad \text{(B8)}$$

Upon quantization, $Q_{n,k}$ and $P_{n,k}$ become operators satisfying the canonical commutation relations $[Q_{n,k},P_{n',k'}]=i\hbar\delta_{n,n'}\delta_{k,k'}$. Introducing creation and annihilation operators

$$Q_{n,k}=\sqrt{\frac{\hbar}{2M\omega_{n,k}}}(a^{\dagger}_{n,k}+a_{n,-k}),$$
$$P_{n,k}=i\sqrt{\frac{\hbar M\omega_{n,k}}{2}}(a^{\dagger}_{n,k}-a_{n,-k}), \quad \text{(B9)}$$

the Hamiltonian assumes the standard second-quantized form

$$\hat{H}_{\rm ph}=\sum_{k,n}\hbar\omega_{n,k}a^{\dagger}_{n,k}a_{n,k}. \quad \text{(B10)}$$

Finally, the quantized displacement field reads

$$\vec{u}(\vec{r})=\sum_{k,n}\sqrt{\frac{\hbar}{2M\omega_{n,k}}}\vec{u}^{\perp}_{n,k}(y,z)(a_{n,k}e^{ikx}+a^{\dagger}_{n,k}e^{-ikx}). \quad \text{(B11)}$$

APPENDIX C: STRAIN COUPLING

The strain-induced coupling between the SiV center and the localized mechanical modes of the phononic crystal defect cavity arises from modifications of the Coulomb potential of the SiV center's electrons caused by lattice displacements in the vicinity of the center. Under the Born-Oppenheimer approximation and for small lattice deformations, the resulting energy shift is linear in the local strain field and can be expressed as [3]

$$\hat{H}_{\rm strain}=\sum_{ij}V_{ij}\epsilon_{ij}. \quad \text{(C1)}$$

Here, V_{ij} is an operator acting on the electronic orbital states of the SiV center, and ϵ_{ij} is the strain tensor defined as

$$\epsilon_{ij}=\frac{1}{2}\left(\frac{\partial u_i}{\partial x_j}+\frac{\partial u_j}{\partial x_i}\right), \quad \text{(C2)}$$

where u_1, u_2, and u_3 denote the quantized displacement-field components along $x_1=x$, $x_2=y$, and $x_3=z$, respectively, at the SiV position [cf. Eq. (B11)]. The coordinate axes follow the convention of the main text, where the SiV center's symmetry axis is aligned along z and the defect cavity extends along x.

The explicit form of the strain-interaction Hamiltonian in the electronic-state basis of the SiV center can be derived by decomposing the strain tensor into the irreducible representations of the D_{3d} point group:

$$\hat{H}_{\rm strain}=\sum_{r}V_r\epsilon_r, \quad \text{(C3)}$$

where r labels the irreducible representations and V_r denotes the corresponding electronic operators. Group-theoretical analysis shows that only the one-dimensional representation A_{1g} and the 2D representation E_g contribute to the coupling [3,49]. Consequently, strain couples independently to the orbital manifolds within each symmetry subspace (e.g., E_g or E_u), while mixing between different manifolds is symmetry forbidden. Restricting the analysis to the ground-state manifold, the relevant strain-coupling terms in Eq. (C3) can be expressed as [3,41]

$$\epsilon_{A_{1g}}=t_{\perp}(\epsilon_{xx}+\epsilon_{yy})+t_{\parallel}\epsilon_{zz},$$
$$\epsilon_{E_{gx}}=d(\epsilon_{xx}-\epsilon_{yy})+f\epsilon_{zx},$$
$$\epsilon_{E_{gy}}=-2d\epsilon_{xy}+f\epsilon_{yz}. \quad \text{(C4)}$$

Here, $t_{\perp},t_{\parallel},d,f$ are the strain susceptibilities with $f/d\sim10^{-4}$, and the subscript g is used to denote the ground-state manifold. The effects of these strain components on the electronic states are described by

$$V_{A_{1g}}=|e_x\rangle\langle e_x|+|e_y\rangle\langle e_y|,$$
$$V_{E_{gx}}=|e_x\rangle\langle e_x|-|e_y\rangle\langle e_y|,$$
$$V_{E_{gy}}=|e_x\rangle\langle e_y|+|e_y\rangle\langle e_x|. \quad \text{(C5)}$$

Because the symmetric local distortion term ($\sim\epsilon_{A_{1g}}$) produces an equal energy shift for all ground-state levels, it does not affect the relative energy splitting relevant to this study and is therefore neglected. Expressing the strain Hamiltonian in the basis of the spin-orbit eigenstates $|e_-\rangle$, $|e_+\rangle$ yields

$$\hat{H}_{\rm strain}=\epsilon_{E_{gx}}(L_-+L_+)-i\epsilon_{E_{gy}}(L_--L_+), \quad \text{(C6)}$$

where $L_+=L^{\dagger}_-=|3\rangle\langle1|+|2\rangle\langle4|$ represents the orbital raising operator within the ground-state manifold. The

corresponding transitions mediated by L_+ and L_- exhibit circular polarization selection rules with respect to the two components of the E_g strain field, reflecting the underlying orbital symmetry of the SiV center.

We consider the configuration where the high-symmetry axis (z) of the SiV center is oriented perpendicular to the phonon propagation direction (x), a geometry that can be experimentally realized in [110]-oriented diamond phononic waveguides. By expanding the local displacement field according to Eq. (B11) and applying the rotating-wave approximation, the effective strain-spin interaction Hamiltonian can be expressed as

$$\hat{H}_{\text{strain}} \simeq \sum_{n,k} \left[\left(g_{n,k} \hat{J}_+^{(1)} + g^*_{n,-k} \hat{J}_+^{(2)} \right) a_{n,k} e^{ikx} + \text{H.c.} \right], \quad \text{(C7)}$$

where $\hat{J}_+^{(1)} = |3\rangle\langle 1|$, $\hat{J}_+^{(2)} = |4\rangle\langle 2|$, and

$$\begin{aligned} g_{n,k} =& d \sqrt{\frac{\hbar k^2}{2\rho V \omega_{n,k}}} \frac{1}{|k|} \left[\left(iku^{\perp,x}_{n,k} + ik \frac{f}{d} \frac{u^{\perp,z}_{n,k}}{2} \right.\right. \\ &+ \left. \frac{f}{d} \frac{\partial_z u^{\perp,x}_{n,k}}{2} - \partial_y u^{\perp,y}_{n,k} \right) \\ &- \left. i \left(iku^{\perp,y}_{n,k} + \partial_y u^{\perp,x}_{n,k} + \frac{f}{d} \frac{\partial_y u^{\perp,z}_{n,k}}{2} + \frac{\partial_z u^{\perp,y}_{n,k}}{2} \right) \right] \\ \equiv& d \sqrt{\frac{\hbar k^2}{2\rho V \omega_{n,k}}} \xi_{n,k}(y,z). \end{aligned} \quad \text{(C8)}$$

Here, $u^{\perp,i}_{n,k}$ denotes the ith component of the transverse displacement profile $\vec{u}^{\perp}_{n,k}(y,z)$, while V denotes the volume of the defect cavity. The first four terms inside the brackets correspond to lattice distortions of E_{g_x} symmetry, while the remaining four represent those of E_{g_y} symmetry.

From Eq. (C7), the circularly polarized selection rules of the SiV center lead to asymmetric coupling for left- and right-propagating phonons, with the directionality reversing when the spin orientation of the involved states is flipped. This asymmetry arises from the opposite ordering of the spin-orbit eigenlevels, where $E_{\downarrow,+} > E_{\downarrow,-}$ but $E_{\uparrow,+} < E_{\uparrow,-}$. However, in this system, the phonon modes are approximately linearly polarized and dominated by the E_{g_x}-type strain, resulting in nearly identical coupling strengths for both propagation directions and spin projections. Thus, the strain-induced interaction can be simplified to

$$\hat{H}_{\text{strain}} \simeq \sum_{n,k} g_{n,k} \hat{J}_+ a_{n,k} e^{ikx} + \text{H.c.} \quad \text{(C9)}$$

Here, $\hat{J}_+ = \hat{J}_+^{(1)} + \hat{J}_+^{(2)} = |3\rangle\langle 1| + |4\rangle\langle 2|$, as in the main text. Unlike the orbital raising operator L_+ above, $\hat{J}_+$ raises the energy in both spin sectors.

To evaluate the bare orbital-phonon coupling strengths of the localized cavity modes, we normalize the finite-element displacement fields to their zero-point amplitudes and project the resulting strain tensors onto the relevant strain channel in the local SiV frame. Here, $\mu \in \{A, B\}$ labels the discrete localized cavity modes, and $g_{k,\mu}$ denotes the coupling g_k of the main text evaluated for mode μ; k is retained only as part of that notation, not as an additional independent mode index. For each localized finite-element eigenmode μ with an arbitrarily scaled displacement field $\vec{U}_\mu(\vec{r})$, the zero-point displacement and strain fields are obtained as

$$\begin{aligned} \mathcal{N}_\mu &= \int_V \rho(\vec{r}) |\vec{U}_\mu(\vec{r})|^2 \, dV, \\ \vec{u}^{\text{zpf}}_\mu(\vec{r}) &= \sqrt{\frac{\hbar}{2\omega_\mu \mathcal{N}_\mu}} \vec{U}_\mu(\vec{r}), \\ \epsilon^{\text{zpf}}_{\mu,ij}(\vec{r}) &= \frac{1}{2} \left(\partial_i u^{\text{zpf}}_{\mu,j}(\vec{r}) + \partial_j u^{\text{zpf}}_{\mu,i}(\vec{r}) \right). \end{aligned}$$

The normalization integrals are evaluated over the physical defect-cavity volume V defined in the main text. For reference, the effective mass is defined as $m_{\text{eff},\mu} = \int_V \rho |\vec{\phi}_\mu|^2 \, dV$, where $\vec{\phi}_\mu = \vec{U}_\mu / \max_V |\vec{U}_\mu|$. This peak-displacement normalization gives $m_{\text{eff},\mu} = \mathcal{N}_\mu / (\max_V |\vec{U}_\mu|)^2$, whereas $M = \rho AL$ above corresponds to the normalization used for the waveguide modes. We assume a [110]-oriented diamond waveguide with the defect-cavity axis $\hat{\mathbf{x}} \parallel [110]$, the SiV symmetry axis $\hat{\mathbf{z}} = \hat{\mathbf{n}}_{\text{SiV}} \parallel [1\bar{1}1]$, and $\hat{\mathbf{y}} \parallel [\bar{1}12]$, forming a right-handed frame. Neglecting the $f\epsilon_{zx}$ contribution and retaining the dominant E_{gx} strain channel, we define the dimensionless projected zero-point strain amplitude at the selected SiV

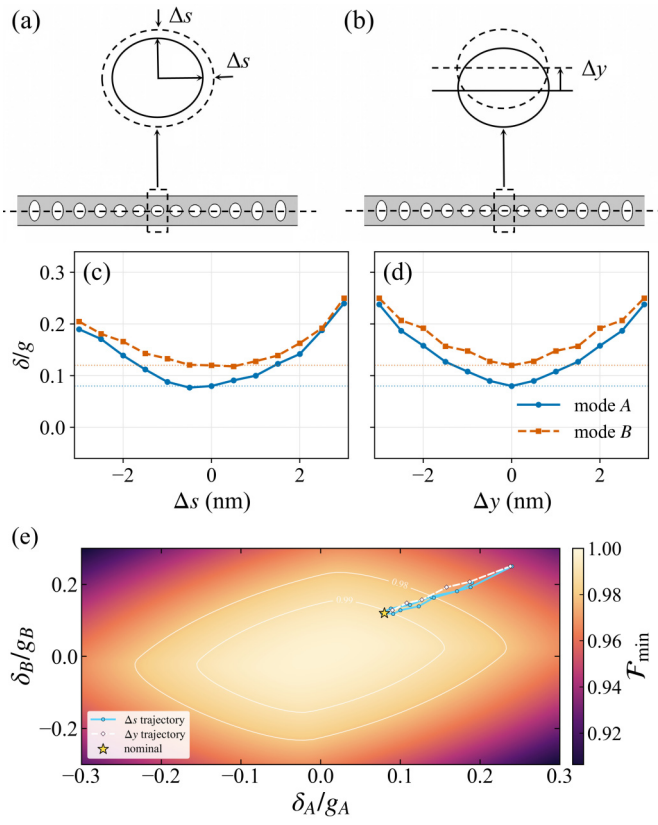


FIG. 8. Fabrication tolerance and detuning robustness. (a), (b) Uniform sidewall offset Δs and transverse position error Δy; solid and dashed lines denote the nominal and perturbed geometries. (c), (d) Normalized detunings of modes A and B vs Δs and Δy, respectively. (e) Minimum transfer fidelity at $G/g = 40$. The curves trace the fabrication-induced detunings, the star marks the zero-error point, and the contours indicate $\mathcal{F}_{\text{min}} = 0.98$ and 0.99.

position $\vec{r}_{\mathrm{SiV}}$ as $\epsilon_\mu^{\mathrm{zpf}} = |\epsilon_{\mu,xx}^{\mathrm{zpf}}(\vec{r}_{\mathrm{SiV}}) - \epsilon_{\mu,yy}^{\mathrm{zpf}}(\vec{r}_{\mathrm{SiV}})|$, with the strain components expressed in the local SiV frame. Unlike $\epsilon_{E_{gx}}$ defined above, $\epsilon_\mu^{\mathrm{zpf}}$ does not include the strain susceptibility d. The coupling magnitude is then $|g_{k,\mu}| = d\epsilon_\mu^{\mathrm{zpf}}$ [12]. We use the strain susceptibility $d/2\pi \approx 1$ PHz/strain specified in the main text. Modes A and B, with $\omega_A/2\pi = 11.941$ GHz and $\omega_B/2\pi = 11.514$ GHz, have effective masses $m_{\mathrm{eff},A} = 319.5$ fg and $m_{\mathrm{eff},B} = 192.8$ fg, respectively. At the selected SiV position, their projected zero-point strains are $\epsilon_A^{\mathrm{zpf}} = 3.07 \times 10^{-8}$ and $\epsilon_B^{\mathrm{zpf}} = 3.22 \times 10^{-8}$. These values give the bare orbital-phonon coupling strengths $|g_{k,A}|/2\pi = 30.7$ MHz and $|g_{k,B}|/2\pi = 32.2$ MHz reported in the main text.

APPENDIX D: EFFECTIVE LOW-ENERGY SPIN-PHONON INTERACTION

For the low-energy interface, we consider the SiV Hamiltonian with transverse Zeeman mixing and static strain. Its two selected dressed eigenstates, $|\widetilde{\downarrow}\rangle$ and $|\widetilde{\uparrow}\rangle$, define the effective spin qubit. The projector onto this subspace is $\hat{P} = |\widetilde{\downarrow}\rangle\langle\widetilde{\downarrow}| + |\widetilde{\uparrow}\rangle\langle\widetilde{\uparrow}|$. For a localized mode μ, projecting the orbital-strain interaction and retaining its resonant spin-flip term gives

$$\hat{H}_{\mathrm{int},\mu} = G_\mu(\hat{\sigma}_+\hat{a}_\mu + \hat{\sigma}_-\hat{a}_\mu^\dagger), \quad G_\mu = \eta_\mu g_{k,\mu}, \tag{D1}$$

where $\hat{\sigma}_+ = |\widetilde{\uparrow}\rangle\langle\widetilde{\downarrow}|$ and $\eta_\mu = |\langle\widetilde{\uparrow}|\hat{J}_+|\widetilde{\downarrow}\rangle|$; the phase of the matrix element is absorbed into the dressed-state basis. The factor $g_{k,\mu}$ is the bare orbital-phonon coupling obtained from the zero-point strain, while η_μ is the orbital matrix element of the dressed spin transition.

In the interaction picture, the exchange term oscillates at $\omega_{\sigma,\mu} - \omega_\mu$ and is resonant when $\omega_{\sigma,\mu} \simeq \omega_\mu$. The bare orbital splitting $\Delta_{\mathrm{SiV}}/2\pi \simeq 46$ GHz enters the dressed states and hence η_μ, but need not match the mechanical-mode frequency.

APPENDIX E: FABRICATION TOLERANCE AND DETUNING ROBUSTNESS

To quantify fabrication imperfections, we vary the uniform sidewall offset Δs and transverse position error Δy independently over $[-3, 3]$ nm. For each perturbed geometry, the effective cavity-waveguide detuning of mode $\mu \in \{A, B\}$, $\delta_\mu = \omega_{+,\mu} + \omega_{-,\mu} - 2\omega'_\mu$, is extracted from the normal-mode triplet and normalized by g_μ. As shown in Figs. 8(c) and 8(d), the normalized detunings remain within $0.077 \leqslant \delta_\mu/g_\mu \leqslant 0.250$.

At $G/g = 40$, we evaluate the detuned triple-swap dynamics using the nominal pulse durations and the open-system model of Fig. 6, minimizing the transfer fidelity over all pure input states of spin 1. At the zero-error point $(\delta_A/g_A, \delta_B/g_B) = (0.08, 0.12)$, Fig. 8(e) gives $\mathcal{F}_{\min} = 0.991$. Along the fabrication-induced trajectories, $\mathcal{F}_{\min} \geqslant 0.986$ for $|\Delta s|, |\Delta y| \leqslant 1$ nm and reaches 0.951 over the full $[-3, 3]$ nm range. Thus, moderate fabrication errors preserve high-fidelity transfer, whereas the largest deviations require postfabrication tuning. Optical-spring tuning demonstrated in diamond optomechanical crystals [54] offers a potential route to compensating residual mechanical-frequency shifts.

Although ω_B lies close to the band edge of waveguide B [Fig. 4(b)], independently varying the sidewall and transverse offsets over $\{-3, -1.5, 0, 1.5, 3\}$ nm yields $g_B/2\pi = \{0.1362, 0.1372, 0.1402, 0.1409, 0.1438\}$ MHz and $\{0.1433, 0.1419, 0.1402, 0.1419, 0.1433\}$ MHz, respectively. Both sets deviate by less than 3% from the nominal value 0.1402 MHz, indicating no substantial coupling enhancement for the tested offsets and preserving $G/g_B \gtrsim 41.7$ for $G/2\pi \simeq 6$ MHz.

[1] M. V. Gustafsson, T. Aref, A. F. Kockum, M. K. Ekström, G. Johansson, and P. Delsing, Propagating phonons coupled to an artificial atom, Science **346**, 207 (2014).

[2] M. J. A. Schuetz, E. M. Kessler, G. Giedke, L. M. K. Vandersypen, M. D. Lukin, and J. I. Cirac, Universal quantum transducers based on surface acoustic waves, Phys. Rev. X **5**, 031031 (2015).

[3] M.-A. Lemonde, S. Meesala, A. Sipahigil, M. J. A. Schuetz, M. D. Lukin, M. Loncar, and P. Rabl, Phonon networks with silicon-vacancy centers in diamond waveguides, Phys. Rev. Lett. **120**, 213603 (2018).

[4] M. C. Kuzyk and H. Wang, Scaling phononic quantum networks of solid-state spins with closed mechanical subsystems, Phys. Rev. X **8**, 041027 (2018).

[5] X. Li, M. C. Kuzyk, and H. Wang, Honeycomblike phononic networks of spins with closed mechanical subsystems, Phys. Rev. Appl. **11**, 064037 (2019).

[6] T. Neuman, M. Eichenfield, M. E. Trusheim, L. Hackett, P. Narang, and D. Englund, A phononic interface between a superconducting quantum processor and quantum networked spin memories, npj Quantum Inf. **7**, 121 (2021).

[7] S. Maity, L. Shao, S. Bogdanović, S. Meesala, Y.-I. Sohn, N. Sinclair, B. Pingault, M. Chalupnik, C. Chia, L. Zheng, K. Lai, and M. Lončar, Coherent acoustic control of a single silicon vacancy spin in diamond, Nat. Commun. **11**, 193 (2020).

[8] B. Kim, H. Kurokawa, K. Sakai, K. Koshino, H. Kosaka, and M. Nomura, Diamond optomechanical cavity with a color center for coherent microwave-to-optical quantum interfaces, Phys. Rev. Appl. **20**, 044037 (2023).

[9] F. Fung, E. Rosenfeld, J. D. Schaefer, A. Kabcenell, J. Gieseler, T. X. Zhou, T. Madhavan, N. Aslam, A. Yacoby, and M. D. Lukin, Toward programmable quantum processors based on spin qubits with mechanically mediated interactions and transport, Phys. Rev. Lett. **132**, 263602 (2024).

[10] A. Iyer, Y. P. Kandel, W. Xu, J. M. Nichol, and W. H. Renninger, Coherent optical coupling to surface acoustic wave devices, Nat. Commun. **15**, 3993 (2024).

[11] K. Kuruma, B. Pingault, C. Chia, M. Haas, G. D. Joe, D. R. Assumpcao, S. W. Ding, C. Jin, C. J. Xin, M. Yeh, N. Sinclair, and M. Lončar, Controlling interactions between high-frequency phonons and single quantum systems using phononic crystals, Nat. Phys. **21**, 77 (2025).

[12] H. Raniwala, P. Anand, S. Krastanov, M. Eichenfield, M. Trusheim, and D. R. Englund, Spin-optomechanical cavity interfaces by deep subwavelength phonon-photon confinement, npj Quantum Inf. **11**, 120 (2025).

[13] P. Rabl, S. J. Kolkowitz, F. H. L. Koppens, J. G. E. Harris, P. Zoller, and M. D. Lukin, A quantum spin transducer based on nanoelectromechanical resonator arrays, Nat. Phys. **6**, 602 (2010).

[14] I. Yeo, P.-L. de Assis, A. Gloppe, E. Dupont-Ferrier, P. Verlot, N. S. Malik, E. Dupuy, J. Claudon, J.-M. Gérard, A. Auffèves, G. Nogues, S. Seidelin, J.-P. Poizat, O. Arcizet, and M. Richard, Strain-mediated coupling in a quantum dot-mechanical oscillator hybrid system, Nat. Nanotechnol. **9**, 106 (2014).

[15] F. J. R. Schülein, E. Zallo, P. Atkinson, O. G. Schmidt, R. Trotta, A. Rastelli, A. Wixforth, and H. J. Krenner, Fourier synthesis of radiofrequency nanomechanical pulses with different shapes, Nat. Nanotechnol. **10**, 512 (2015).

[16] M. Weiß and H. J. Krenner, Interfacing quantum emitters with propagating surface acoustic waves, J. Phys. D: Appl. Phys. **51**, 373001 (2018).

[17] D. Wigger, M. Weiß, M. Lienhart, K. Müller, J. J. Finley, T. Kuhn, H. J. Krenner, and P. Machnikowski, Resonance-fluorescence spectral dynamics of an acoustically modulated quantum dot, Phys. Rev. Res. **3**, 033197 (2021).

[18] R. A. DeCrescent, Z. Wang, P. Imany, R. C. Boutelle, C. A. McDonald, T. Autry, J. D. Teufel, S. W. Nam, R. P. Mirin, and K. L. Silverman, Large single-phonon optomechanical coupling between quantum dots and tightly confined surface acoustic waves in the quantum regime, Phys. Rev. Appl. **18**, 034067 (2022).

[19] C. Spinnler, G. N. Nguyen, Y. Wang, L. Zhai, A. Javadi, M. Erbe, S. Scholz, A. D. Wieck, A. Ludwig, P. Lodahl, L. Midolo, and R. J. Warburton, A single-photon emitter coupled to a phononic-crystal resonator in the resolved-sideband regime, Nat. Commun. **15**, 9509 (2024).

[20] T. Descamps, T. Schetelat, J. Gao, P. J. Poole, D. Dalacu, A. W. Elshaari, and V. Zwiller, Acoustic modulation of individual nanowire quantum dots integrated into a hybrid thin-film lithium niobate photonic platform, Nano Lett. **24**, 12493 (2024).

[21] U. von Lüpke, I. C. Rodrigues, Y. Yang, M. Fadel, and Y. Chu, Engineering multimode interactions in circuit quantum acoustodynamics, Nat. Phys. **20**, 564 (2024).

[22] Y. W. Chu, P. Kharel, W. H. Renninger, L. D. Burkhart, L. Frunzio, P. T. Rakich, and R. J. Schoelkopf, Quantum acoustics with superconducting qubits, Science **358**, 199 (2017).

[23] A. Bienfait, K. J. Satzinger, Y. P. Zhong, H.-S. Chang, M.-H. Chou, C. R. Conner, É. Dumur, J. Grebel, G. A. Peairs, R. G. Povey, and A. N. Cleland, Phonon-mediated quantum state transfer and remote qubit entanglement, Science **364**, 368 (2019).

[24] M. Kounalakis, Y. M. Blanter, and G. A. Steele, Synthesizing multi-phonon quantum superposition states using flux-mediated three-body interactions with superconducting qubits, npj Quantum Inf. **5**, 100 (2019).

[25] J. M. Kitzman, J. R. Lane, C. Undershute, P. M. Harrington, N. R. Beysengulov, C. A. Mikolas, K. W. Murch, and J. Pollanen, Phononic bath engineering of a superconducting qubit, Nat. Commun. **14**, 3910 (2023).

[26] W. J. M. Franse, C. A. Potts, V. A. S. V. Bittencourt, A. Metelmann, and G. A. Steele, High-coherence quantum acoustics with planar superconducting qubits, Appl. Phys. Lett. **125**, 183501 (2024).

[27] P.-B. Li, Y. Zhou, W.-B. Gao, and F. Nori, Enhancing spin-phonon and spin-spin interactions using linear resources in a hybrid quantum system, Phys. Rev. Lett. **125**, 153602 (2020).

[28] Y. Zhou, C.-S. Hu, D.-Y. Lü, X.-K. Li, H.-M. Huang, Y.-C. Xiong, and X.-Y. Lü, Synergistic enhancement of spin–phonon interaction in a hybrid system, Photonics Res. **10**, 1640 (2022).

[29] K. W. Lee, D. Lee, P. Ovartchaiyapong, J. Minguzzi, J. R. Maze, and A. C. Bleszynski Jayich, Strain coupling of a mechanical resonator to a single quantum emitter in diamond, Phys. Rev. Appl. **6**, 034005 (2016).

[30] D. A. Golter, T. Oo, M. Amezcua, I. Lekavicius, K. A. Stewart, and H. L. Wang, Coupling a surface acoustic wave to an electron spin in diamond via a dark state, Phys. Rev. X **6**, 041060 (2016).

[31] D. Lee, K. W. Lee, J. V. Cady, P. Ovartchaiyapong, and A. C. B. Jayich, Topical review: Spins and mechanics in diamond, J. Opt. **19**, 033001 (2017).

[32] H. Y. Chen, E. R. MacQuarrie, and G. D. Fuchs, Orbital state manipulation of a diamond nitrogen-vacancy center using a mechanical resonator, Phys. Rev. Lett. **120**, 167401 (2018).

[33] B. Pingault, J. N. Becker, C. H. H. Schulte, C. Arend, C. Hepp, T. Godde, A. I. Tartakovskii, M. Markham, C. Becher, and M. Atatüre, All-optical formation of coherent dark states of silicon-vacancy spins in diamond, Phys. Rev. Lett. **113**, 263601 (2014).

[34] X.-L. Dong, P.-B. Li, T. Liu, and F. Nori, Unconventional quantum sound-matter interactions in spin-optomechanical-crystal hybrid systems, Phys. Rev. Lett. **126**, 203601 (2021).

[35] X.-L. Dong, C.-P. Shen, S.-Y. Gao, H.-R. Li, H. Gao, F.-L. Li, and P.-B. Li, Chiral spin-phonon bound states and spin-spin interactions with phononic lattices, Phys. Rev. Res. **4**, 023077 (2022).

[36] A. L. Falk, B. B. Buckley, G. Calusine, W. F. Koehl, V. V. Dobrovitski, A. Politi, C. A. Zorman, P. X. -L. Feng, and D. D. Awschalom, Polytype control of spin qubits in silicon carbide, Nat. Commun. **4**, 1819 (2013).

[37] M. S. J. Barson, P. Peddibhotla, P. Ovartchaiyapong, K. Ganesan, R. L. Taylor, M. Gebert, Z. Mielens, B. Koslowski, D. A. Simpson, L. P. McGuinness, J. McCallum, S. Prawer, S. Onoda, T. Ohshima, A. C. Bleszynski Jayich, F. Jelezko, N. B. Manson, and M. W. Doherty, Nanomechanical sensing using spins in diamond, Nano Lett. **17**, 1496 (2017).

[38] S. J. Whiteley, G. Wolfowicz, C. P. Anderson, A. Bourassa, H. Ma, M. Ye, G. Koolstra, K. J. Satzinger, M. V. Holt, F. J. Heremans, A. N. Cleland, D. I. Schuster, G. Galli, and D. D. Awschalom, Spin-phonon interactions in silicon carbide addressed by Gaussian acoustics, Nat. Phys. **15**, 490 (2019).

[39] Y. I. Sohn, S. Meesala, B. Pingault, H. A. Atikian, J. Holzgrafe, M. Gündoğan, C. Stavrakas, M. J. Stanley, A. Sipahigil, J. Choi, M. Zhang, J. L. Pacheco, J. Abraham, E. Bielejec, M. D. Lukin, M. Atatüre, and M. Lončar, Controlling the coherence of a diamond spin qubit through its strain environment, Nat. Commun. **9**, 2012 (2018).

[40] K. V. Kepesidis, M. A. Lemonde, A. Norambuena, J. R. Maze, and P. Rabl, Cooling phonons with phonons: Acoustic reservoir-engineering with silicon-vacancy centers in diamond, Phys. Rev. B **94**, 214115 (2016).

[41] S. Meesala, Y. I. Sohn, B. Pingault, L. Shao, H. A. Atikian, J. Holzgrafe, M. Gündoğan, C. Stavrakas, A. Sipahigil, C. Chia, R. Evans, M. J. Burek, M. Zhang, L. Wu, J. L. Pacheco, J. Abraham, E. Bielejec, M. D. Lukin, M. Atatüre, and M. Lončar, Strain engineering of the silicon-vacancy center in diamond, Phys. Rev. B **97**, 205444 (2018).

[42] M. S. Kushwaha, P. Halevi, G. Martínez, L. Dobrzynski, and B. Djafari-Rouhani, Theory of acoustic band structure of periodic elastic composites, Phys. Rev. B **49**, 2313 (1994).

[43] M. Eichenfield, J. Chan, R. M. Camacho, K. J. Vahala, and O. Painter, Optomechanical crystals, Nature (London) **462**, 78 (2009).

[44] C. Monroe and J. Kim, Scaling the ion trap quantum processor, Science **339**, 1164 (2013).

[45] D. Hatanaka, I. Mahboob, K. Onomitsu, and H. Yamaguchi, Phonon waveguides for electromechanical circuits, Nat. Nanotechnol. **9**, 520 (2014).

[46] A. Sipahigil, R. E. Evans, D. D. Sukachev, M. J. Burek, J. Borregaard, M. K. Bhaskar, C. T. Nguyen, J. L. Pacheco, H. A. Atikian, C. Meuwly, R. M. Camacho, F. Jelezko, E. Bielejec, H. Park, M. Lončar, and M. D. Lukin, An integrated diamond nanophotonics platform for quantum-optical networks, Science **354**, 847 (2016).

[47] R. E. Evans, M. K. Bhaskar, D. D. Sukachev, C. T. Nguyen, A. Sipahigil, M. J. Burek, B. Machielse, G. H. Zhang, A. S. Zibrov, E. Bielejec, H. Park, M. Lončar, and M. D. Lukin, Photon-mediated interactions between quantum emitters in a diamond nanocavity, Science **362**, 662 (2018).

[48] C. Hepp, T. Müller, V. Waselowski, J. N. Becker, B. Pingault, H. Sternschulte, D. Steinmüller-Nethl, A. Gali, J. R. Maze, M. Atatüre, and C. Becher, Electronic structure of the silicon vacancy color center in diamond, Phys. Rev. Lett. **112**, 036405 (2014).

[49] C. Hepp, Electronic structure of the silicon vacancy color center in diamond, Ph.D. thesis, University of Saarland, 2014.

[50] A. N. Cleland, *Foundations of Nanomechanics* (Springer, Germany, 2002).

[51] J.-Q. Chen, Y.-F. Qiao, X.-L. Dong, X.-L. Hei, and P.-B. Li, Dissipation-assisted preparation of steady spin-squeezed states of SiV centers, Phys. Rev. A **103**, 013709 (2021).

[52] J. R. Schrieffer and P. A. Wolff, Relation between the Anderson and Kondo Hamiltonians, Phys. Rev. **149**, 491 (1966).

[53] J. Chan, A. H. Safavi-Naeini, J. T. Hill, S. Meenehan, and O. Painter, Optimized optomechanical crystal cavity with acoustic radiation shield, Appl. Phys. Lett. **101**, 081115 (2012).

[54] M. J. Burek, J. D. Cohen, S. M. Meenehan, N. El-Sawah, C. Chia, T. Ruelle, S. Meesala, J. Rochman, H. A. Atikian, M. Markham, D. J. Twitchen, M. D. Lukin, O. Painter, and M. Lončar, Diamond optomechanical crystals, Optica **3**, 1404 (2016).

[55] G. S. MacCabe, H. Ren, J. Luo, J. D. Cohen, H. Zhou, A. Sipahigil, M. Mirhosseini, and O. Painter, Nano-acoustic resonator with ultralong phonon lifetime, Science **370**, 840 (2020).

[56] D. S. Levonian, R. Riedinger, B. Machielse, E. N. Knall, M. K. Bhaskar, C. M. Knaut, R. Bekenstein, H. Park, M. Lončar, and M. D. Lukin, Optical entanglement of distinguishable quantum emitters, Phys. Rev. Lett. **128**, 213602 (2022).

[57] P.-L. Yu, K. Cicak, N. S. Kampel, Y. Tsaturyan, T. P. Purdy, R. W. Simmonds, and C. A. Regal, A phononic bandgap shield for high-Q membrane microresonators, Appl. Phys. Lett. **104**, 023510 (2014).

[58] R. N. Patel, Z. Y. Wang, W. Jiang, C. J. Sarabalis, J. T. Hill, and A. H. Safavi-Naeini, Single-mode phononic wire, Phys. Rev. Lett. **121**, 040501 (2018).

[59] S. M. Meenehan, J. D. Cohen, G. S. MacCabe, F. Marsili, M. D. Shaw, and O. Painter, Pulsed excitation dynamics of an optomechanical crystal resonator near its quantum ground state of motion, Phys. Rev. X **5**, 041002 (2015).

[60] Y. Tsaturyan, A. Barg, E. S. Polzik, and A. Schliesser, Ultracoherent nanomechanical resonators via soft clamping and dissipation dilution, Nat. Nanotechnol. **12**, 776 (2017).

[61] G. Huang, A. Beccari, N. J. Engelsen, and T. J. Kippenberg, Room-temperature quantum optomechanics using an ultralow noise cavity, Nature (London) **626**, 512 (2024).

[62] T. J. Clark, S. Bernard, J. Ma, V. Dumont, and J. C. Sankey, Optically defined phononic crystal defect, Phys. Rev. Lett. **133**, 226904 (2024).

[63] C. H. Dong, Y. D. Wang, and H. L. Wang, Optomechanical interfaces for hybrid quantum networks, Natl. Sci. Rev. **2**, 510 (2015).

[64] H.-K. Lau and A. A. Clerk, Ground-state cooling and high-fidelity quantum transduction via parametrically driven bad-cavity optomechanics, Phys. Rev. Lett. **124**, 103602 (2020).

[65] J. Zhang, C. Zhu, C. Wolff, and B. Stiller, Quantum coherent control in pulsed waveguide optomechanics, Phys. Rev. Res. **5**, 013010 (2023).

[66] B. Vermersch, P. O. Guimond, H. Pichler, and P. Zoller, Quantum state transfer via noisy photonic and phononic waveguides, Phys. Rev. Lett. **118**, 133601 (2017).

[67] X.-X. Li, B. Li, and P.-B. Li, Simulation of topological phases with color center arrays in phononic crystals, Phys. Rev. Res. **2**, 013121 (2020).

[68] D. D. Sukachev, A. Sipahigil, C. T. Nguyen, M. K. Bhaskar, R. E. Evans, F. Jelezko, and M. D. Lukin, Silicon-vacancy spin qubit in diamond: A quantum memory exceeding 10 ms with single-shot state readout, Phys. Rev. Lett. **119**, 223602 (2017).

[69] H. Ren, M. H. Matheny, G. S. MacCabe, J. Luo, H. Pfeifer, M. Mirhosseini, and O. Painter, Two-dimensional optomechanical crystal cavity with high quantum cooperativity, Nat. Commun. **11**, 3373 (2020).

[70] Y. D. Wang and A. A. Clerk, Using dark modes for high-fidelity optomechanical quantum state transfer, New J. Phys. **14**, 105010 (2012).

[71] A. Uhlmann, The transition probability in the state space of a $*$-algebra, Rep. Math. Phys. **9**, 273 (1976).